An accurate sharp interface method for two-phase compressible flows at low-mach regime

Ziqiang Zou, Edouard Audit, Nicolas Grenier, Christian Tenaud

Flow, Turbulence and Combusion manuscript No.
(will be inserted by the editor)

An accurate sharp interface method for two-phase compressible flows at low-Mach regime.

Ziqiang Zou · Edouard Audit · Nicolas Grenier · Christian Tenaud

Received: date / Accepted: date

Abstract An accurate numerical approach is presented for computing two-phase flows with surface tension at low-Mach regime. To develop such a model, where slight compressible effects are taken into account as well as correct thermodynamical closures, both the liquid and the gas are considered compressible and described by a precise compressible solver. A low-Mach correction has been implemented to eliminate excessive numerical dissipation. The interface between two-phase flows is captured by the level set method that is considered to be sharp. The interface capturing issue of the level set method within the Eulerian framework is the key point of the two-phase flow simulations, and in this work we propose a high-order coupled time-space approach for interface advection. Several numerical test-cases have been employed to validate the present numerical approach and enlighten its good performance.

Keywords two-phase flows · compressible flows · level set method · ghost fluid method · surface tension · low-Mach correction

1 Introduction

Two-phase non-miscible flows can take a large variety of forms and are encountered in a wide range of natural and industrial processes: their modeling is at the heart of numerous studies and it is necessary to accurately describe the interface.

There are basically two different approaches to model non-miscible two-phase flows, the diffuse interface method and the sharp interface method. For the first approach, the interface is represented by a smooth internal layer. An artificial

Ziqiang Zou E-mail: ziqiang.zou@cea.fr · Edouard Audit
Maison de la Simulation, CEA, CNRS, Univ. Paris-Sud, UVSQ, Univ. Paris-Saclay, Gif-sur-Yvette, France

Nicolas Grenier · Christian Tenaud
LIMSI, CNRS, Univ. Paris-Sud, Univ. Paris-Saclay, Orsay, France

mixture state occurs in this layer and may cause some inconvenient and non-physical results. The second approach can avoid this mixing state by representing the interface as a contact discontinuity. Fluids in different regions separated by an interface are described by different single-phase equations of state. In the present study, we concentrate on this sharp interface method.

In the framework of sharp interface, several strategies are available to predict the interface motion: front tracking (FT) method [35], volume of fluid (VOF) method [16], level set method [28]. FT method is based on the Lagrangian tracking of the interface with an unstructured mesh. Although this approach has some advantages such as explicit representation and Lagrangian transport of the interface, this method requires frequent mesh rearrangements because of interface motion that is an obvious shortcoming. This procedure could be complex especially when the interface suffers from significant deformations. Keeping some homogeneity of distribution of markers on the interface (nodes of the unstructured mesh) as well as tackling interface break-up and coalescence could also be a big challenge. VOF method is an Eulerian approach based on a scalar field representing the volume fraction of a fluid inside a control volume. The interface is then represented implicitly. This approach can avoid mesh rearrangement issues and overcome difficulties of the FT method, but numerical diffusion in the transport scheme could cause non-physical smearing of the interface leading to a loss of accuracy. The level set method is based on a signed distance function to the interface which is described by the zero iso-contour of this continuous function. The level set method has an important advantage on interface geometry estimation such as normal vector and curvature. Although the evolution of this function follows simple Eulerian scalar transport and the function is continuous, this method generally can not guarantee mass conservation, even if transport relies on high-order accuracy schemes. To circumvent this issue, several approaches have been proposed, such as level set-VOF coupling technique (CLSVOF) [24], accurate conservative level set technique (ACLS) [9], particle level set method (PLS) [10], cut-cell technique [19] and adaptive mesh refinement (AMR) approach [26]. The existence of these techniques shows good compatibility with the level set method.

Considering good geometric properties presented by the level set method, we selected this method to implicitly represent interface in Eulerian framework. While focusing in the present study on the coupling of this method with low-Mach compressible solver, we keep mass conservation issue in background for further investigations.

Flows of interest contain one liquid phase and one gas phase separated by an interface. As the Mach number in liquid is generally small, there are generally two different approaches for liquid modeling: incompressible approach [22, 27, 33] and compressible approach [11, 17, 18, 23].

Incompressible approach is the most natural approach to simulate single-phase flows without any density variations. Then some extensions [30] have been derived to take into account some variable density effects and dilatability (to model natural convection effects in gas for example). However, hypothesis to close equations are more restrictive on gas model (equation of state).

While in incompressible approach, the low-Mach regime is more an issue of extension of the physical model under correct assumptions, in the compressible approach this low-Mach regime is formally correctly handled by the physical description but its numerical design is far more difficult.

Classical numerical compressible solvers used in the low-Mach regime face two known issues. Firstly, when the flow is slow compared to sound speed, common compressible solvers lose accuracy due to excessive numerical dissipation [8]. Secondly, stability condition requires very restrictive time steps for explicit schemes due to the importance of acoustic speed of sound compared to advective velocity.

To overcome this issue while keeping possibilities to propose accurate modelling of fluid equation of state (liquid or gas) to best match thermodynamical behavior, we decide to model these two-phase flows in low-Mach regime with a full compressible approach with a new solver called "all regime Lagrange-Projection like numerical scheme" for the description of each pure phase. The key idea is to decouple the acoustic and transport phenomenon and then alter the numerical flux in the acoustic approximation to obtain a uniform truncation error in terms of Mach number [3]. For the near-equilibrium problem, we propose a well-balanced scheme to preserve the equilibrium state by giving an accurate discretization of the non-conservative terms (gravity [4] and surface tension effects).

To address the issue of modelling two-phase flows in the low-Mach regime with an accurate description of the interface, we propose to combine this new compressible solver with a sharp interface model. The interface is treated as a contact discontinuity and is captured by the level set method. Coupling between the fluids of different phases at the interface have been realized by the ghost fluid method [12].

2 Governing equations for two-phase compressible flow

The dynamics of a compressible flow containing two immiscible fluids is governed by following the compressible Navier-Stokes equations:

$$\begin{cases} \rho_t + \nabla\cdot(\rho\mathbf{u}) = 0, \\ (\rho\mathbf{u})_t + \nabla\cdot(\rho\mathbf{u}\otimes\mathbf{u}) + \nabla p = \rho\mathbf{g} + \nabla\cdot\tau_{\mathrm{v}} + S_{st}, \\ (\rho E)_t + \nabla\cdot((\rho E + p)\mathbf{u}) = \rho\mathbf{g}\cdot\mathbf{u} + \nabla\cdot(\tau_{\mathrm{v}}\mathbf{u}) + \mathbf{u}\cdot S_{st} + \nabla\cdot(\mathcal{K}\nabla T), \end{cases} \tag{1}$$

where ρ is the density, $\mathbf{u}$ is the fluid velocity vector, p is the fluid pressure, $\mathcal{K}$ is the thermal conductivity, T is the fluid temperature, $\tau_{\mathrm{v}} = \mu\left(\nabla\mathbf{u} + (\nabla\mathbf{u})^T\right) - \frac{2}{3}\mu\nabla\cdot\mathbf{u}\mathcal{I}$ is the viscous stress tensor following the Stokes hypothesis, $\mathbf{g}$ is the gravity acceleration and S_{st} is the source term associated with capillary effects. E denotes the total energy per unit of mass which is related to the specific internal energy e via $E = e + \frac{1}{2}|\mathbf{u}|^2$.

This system is closed by adding an equation of state (EOS). For non-miscible two phase flows, to avoid the mixture at the interface, each cell is completely treated as a cell of phase 1 or phase 2. Here we use the general EOS in the Mie-Gruneisen form [14,32] for both fluids 1 and 2 to link the pressure to the internal energy and the density:

$$\rho e = \frac{p + \gamma p^{\infty}}{\gamma - 1}, \tag{2}$$

$$\rho(\gamma - 1)C_v T = p + p^{\infty} \tag{3}$$

and for each fluid, the sound speed can be given by:

$$c^2 = \gamma\frac{p + p^{\infty}}{\rho}, \tag{4}$$

where γ is the heat capacity ratio ($\gamma = C_p/C_v$), C_p and C_v are the heat capacities at constant pressure and heat capacity at constant volume respectively. p^∞ is a constant pressure, representing the molecular attraction between fluid molecules.

The interface of the two-phase flows is captured by a level set method [28]. As the interface is advected passively by the fluid velocity field, the evolution of the signed distance function ϕ can be given by a linear hyperbolic advection equation:

$$\phi_t + \mathbf{u} \cdot \nabla \phi = 0. \tag{5}$$

Surface tension effects are modeled by Laplace equation which links the pressure jump at the interface between fluids 1 and 2, σ the surface tension coefficient and κ the curvature of the interface:

$$p_1 - p_2 = \sigma\kappa. \tag{6}$$

To insert this relation into (1), the classical approach [2] is to transform this Laplace surface condition into a volumic constraint into S_{st}:

$$S_{st} = \sigma\kappa\mathbf{n}\delta\left(\phi\right) \tag{7}$$

where $\delta(\phi)$ is the surface Dirac function which is non-zero only on the interface. The normal vector $\mathbf{n}$ and the interface curvature κ at the interface are deduced from the distance function by the following relations:

$$\mathbf{n} = \nabla\phi/|\nabla\phi|_{\phi=0}, \quad \kappa = \nabla \cdot \left(\frac{\nabla\phi}{|\nabla\phi|}\right)_{\phi=0}. \tag{8}$$

3 Numerical method

In this section, we present the numerical scheme to solve the system within the Eulerian framework. Since the approach is based on a sharp interface (which avoids numerical diffusion), each cell is completely treated as a cell of fluid 1 or of fluid 2, so the phase interface is shifted to the grid cell boundary of the nearest neighboring grid cell [11]. This study is limited to uniform cartesian meshes.

To solve the global system formed by the set of equations (1 to 5), we first introduce the method for the bulk flow. Then, we explain the strategy for two-phase coupling via the ghost fluid method [12]. As the surface tension exists only at the interface, it is not required to take terms linked with surface tension effect into account for the bulk flow.

3.1 Numerical method for the bulk flow without surface tension

For numerical purposes, the particular form of the system adopted depends largely on the numerical technique to be used to solve this system. One possible approach is to split the advection effects from the diffusion during a small time interval [34],

so the global system can be divided into an Euler system with gravitational source term:

$$\begin{cases} \rho_t + \nabla\cdot(\rho\mathbf{u}) = 0, \\ (\rho\mathbf{u})_t + \nabla\cdot(\rho\mathbf{u}\otimes\mathbf{u}) + \nabla p = \rho\mathbf{g}, \\ (\rho E)_t + \nabla\cdot((\rho E + p)\mathbf{u}) = \rho\mathbf{g}\cdot\mathbf{u}, \\ \phi_t + \mathbf{u}\cdot\nabla\phi = 0, \end{cases} \tag{9}$$

and a diffusion system:

$$\begin{cases} \rho_t = 0, \\ (\rho\mathbf{u})_t = \nabla\cdot\tau_{\mathrm{v}}, \\ (\rho E)_t = \nabla\cdot(\tau_{\mathrm{v}}\mathbf{u}) + \nabla\cdot(\mathcal{K}\nabla T), \\ \phi_t = 0. \end{cases} \tag{10}$$

To solve such a system presented in (9), by following and extending the work of [3], we explain in next section the acoustic splitting of an Euler system. The gravitational source term is added later to the Euler system.

3.1.1 Acoustic splitting

During a small time interval, the Euler equations are split to decouple fast acoustic waves from slow material motion and two subsystems are obtained:

- on one hand, we have an acoustic subsystem:

$$\begin{cases} \rho_t + \rho\nabla\cdot(\mathbf{u}) = 0, \\ (\rho\mathbf{u})_t + \rho\mathbf{u}\nabla\cdot\mathbf{u} + \nabla p = 0, \\ (\rho E)_t + \rho E\nabla\cdot\mathbf{u} + \nabla\cdot(p\mathbf{u}) = 0, \\ \phi_t = 0, \end{cases} \tag{11}$$

  with characteristic wave velocity: $\lambda_\omega^0 = 0, \lambda_\omega^+ = c, \lambda_\omega^- = -c$.
- While, on the other hand, it remains the transport subsystem:

$$\begin{cases} \rho_t + \mathbf{u}\cdot\nabla\rho = 0, \\ (\rho\mathbf{u})_t + (\mathbf{u}\cdot\nabla)\rho\mathbf{u} = 0, \\ (\rho E)_t + \mathbf{u}\cdot\nabla(\rho E) = 0, \\ \phi_t + \mathbf{u}\cdot\nabla\phi = 0, \end{cases} \tag{12}$$

  with characteristic velocity in direction $\boldsymbol{\omega}$: $\lambda_\omega^{0,\pm} = \mathbf{u}\cdot\boldsymbol{\omega}$.

3.1.2 Well-balanced scheme for external source term

When we want to study a dynamical phenomenon near equilibrium, special treatment of the source term is necessary to guarantee that the equilibrium state can be preserved. A way to overcome this issue is to treat the source term $\mathbf{g}$ with a well-balanced scheme.

A well-balanced scheme aims at preserving discrete versions of some continuous equilibrium states. It means that the scheme has its version of equilibrium

and it is able to preserve it around machine precision. We follow the work of [4] which derived a well-balanced scheme for the Saint-Venant equations and add well-chosen terms in the scheme to exactly compensate hydrostatic pressure gradients at equilibrium.

To obtain such equilibrium, we need to determine a pressure to balance the gravity. A natural way is to include the external source term into the acoustic subsystem:

$$\begin{cases} \rho_t + \rho\nabla\cdot\mathbf{u} = 0, \\ (\rho\mathbf{u})_t + \rho\mathbf{u}\nabla\cdot\mathbf{u} + \nabla p = -\rho\nabla\psi, \\ (\rho E)_t + \rho E\nabla\cdot\mathbf{u} + \nabla\cdot(p\mathbf{u}) = -\rho\mathbf{u}\cdot\nabla\psi, \\ \phi_t = 0, \end{cases} \tag{13}$$

where ψ is the gravitational potential and $\mathbf{g} = -\nabla\psi$. For hydrostatic balance, the flow is at rest and the gravitational force is balanced by the pressure. This hydrostatic balance can be expressed as:

$$\nabla p = -\rho\nabla\psi, \quad \mathbf{u} = \mathbf{0}. \tag{14}$$

Given a fluid state $(\rho, \rho\mathbf{u}, \rho E, \phi)_j^n$, this splitting algorithm can be decomposed as follows:

- Update the fluid state $(\rho, \rho\mathbf{u}, \rho E, \phi)_j^n$ to the value $(\rho, \rho\mathbf{u}, \rho E, \phi)_j^{n+}$ by approximating the solution of the acoustic subsystem (13).
- Update the fluid state $(\rho, \rho\mathbf{u}, \rho E, \phi)_j^{n+}$ to the value $(\rho, \rho\mathbf{u}, \rho E, \phi)_j^{n+1-}$ by approximating the solution of the transport subsystem (12).
- Update the fluid state $(\rho, \rho\mathbf{u}, \rho E, \phi)_j^{n+1-}$ to the value $(\rho, \rho\mathbf{u}, \rho E, \phi)_j^{n+1}$ by approximating the solution of the diffusion subsystem (10).

In the next subsections, we present the numerical discretization of the system for the bulk flows.

3.1.3 Acoustic subsystem discretization

The acoustic subsystem (13) is a quasilinear system. In order to derive the resolution of this subsystem, we will perform several approximations. We notice that for a smooth solution in (13), we also have $\partial_t(p/(\rho c)^2) + \tau\nabla\cdot\mathbf{u} = 0$ (see [1]). We thus choose to perform a Suliciu-type approximation of (13) by introducing a surrogate pressure π and considering the following relaxed system (with variable change $\tau = 1/\rho$):

$$\begin{cases} \partial_t\tau - \tau\nabla\cdot\mathbf{u} = 0, \\ \partial_t\mathbf{u} + \tau\nabla\pi = -\nabla\psi, \\ \partial_t E + \tau\nabla\cdot(\pi u) = -\mathbf{u}\cdot\nabla\psi, \\ (\pi/a^2)_t + \tau\nabla\cdot\mathbf{u} = \chi(p-\pi), \\ a_t = 0, \\ \phi_t = 0, \end{cases} \tag{15}$$

$a > 0$ and its definition will be given later. In the regime $\chi \to \infty$, we formally recover (13). In our numerical solver context, we classically mimic the $\chi \to \infty$ regime enforcing at each time step $\pi_i^n = p^{EOS}(\tau_i^n, e_i^n)$ as in (2) and then solving

(15) with $\chi = 0$. Then it is easier to find the solution of the associated Riemann problem in each direction. We solve (13) by following classical finite volume method applied to cell j:

$$\begin{cases} L_j \rho_j^{n+} = \rho_j^n, \\ L_j \left(\rho \mathbf{u}\right)_j^{n+} = (\rho \mathbf{u})_j^n - \Delta t \sum\limits_{k \in \mathcal{N}(j)} \mathcal{L}_{jk} \pi_{jk}^* \mathbf{n}_{jk} - \Delta t (\rho \nabla \Psi)_j^n, \\ L_j \left(\rho E\right)_j^{n+} = (\rho E)_i^n - \Delta t \sum\limits_{k \in \mathcal{N}(j)} \mathcal{L}_{jk} \pi_{jk}^* u_{jk}^* - \Delta t \mathbf{u} \cdot (\rho \nabla \Psi)_j^n, \\ \phi_j^{n+} = \phi_j^n, \\ L_j = 1 + \Delta t \left(\sum\limits_{k \in \mathcal{N}(j)} \mathcal{L}_{jk} u_{jk}^* \right), \end{cases} \tag{16}$$

where cell k is the neighbor of cell j. $\mathcal{L}_{jk} = |\Gamma_{jk}|/|\Omega_j|$, where Γ_{jk} and Ω_j are respectively the face area between cell j and cell k and the volume of cell j. We define $\mathcal{N}(j)$ the set of indices k such that $\mathcal{L}_{jk}$ is a face of Ω_j. The scalar quantities π_{jk}^* and u_{jk}^* respectively represent the intermediate pressure and normal velocity at the face Γ_{jk} of a Riemann problem associated with the approximate system (15). To keep the equilibrium state presented in (14), π_{jk}^* and u_{jk}^* can be expressed as:

$$\begin{aligned} u_{jk}^* &= \frac{\mathbf{n}_{jk} \cdot (a_j \mathbf{u}_j^{\#} + a_k \mathbf{u}_k^{\#})}{a_j + a_k} - \frac{\pi_k^{\#} - \pi_j^{\#} + \frac{(\rho_j + \rho_k)}{2}(\Psi_k - \Psi_j)}{(a_j + a_k)}, \\ \pi_{jk}^* &= \frac{a_k \pi_j^{\#} + a_j \pi_k^{\#} + \frac{a_j - a_k}{2}\frac{(\rho_j + \rho_k)}{2}(\Psi_k - \Psi_j)}{a_j + a_k} - \frac{a_j a_k \theta_{jk}}{a_j + a_k} \mathbf{n}_{jk} \cdot (\mathbf{u}_k^{\#} - \mathbf{u}_j^{\#}). \end{aligned} \tag{17}$$

For more details about the approximate Riemann solver and well-balanced scheme for the gravitational force, please refer to the section 3.2.1 and the work of [29] respectively. The parameter a is an approximation of ρc and must complies with the subcharacteristic condition that preserves positiveness of density [1]. With relaxation speeds defined in [1], the parameter a can be set as followings:

$$a_j = \mathbb{K} \rho_j \max(c_k, c_j), \quad a_k = \mathbb{K} \rho_k \max(c_k, c_j), \tag{18}$$

where $\mathbb{K} \geq 1$. In the present study, the value of $\mathbb{K}$ is set to be 1.1 which is more than enough to satisfy the subcharacteristic condition at low-Mach regime.

The term concerning the external source is cell centered on a uniform cartesian mesh (see [4]) and its discretization is:

$$\begin{aligned} (\rho \nabla \Psi)_j &= \frac{1}{2} \sum_{k \in \mathcal{N}(j)} (\rho \nabla \psi)_{jk} = \frac{1}{2} \sum_{k \in \mathcal{N}(j)} \mathcal{L}_{jk} \frac{(\rho_j + \rho_k)}{2} (\Psi_k - \Psi_j) \mathbf{n}_{jk}, \\ \mathbf{u} \cdot (\rho \nabla \Psi)_j &= \frac{1}{2} \sum_{k \in \mathcal{N}(j)} \mathcal{L}_{jk} \frac{(\rho_j + \rho_k)}{2} (\Psi_k - \Psi_j) u_{jk}^*. \end{aligned} \tag{19}$$

In (17), superscript # gives us two choices, either $\# = n$ for an explicit acoustic time integration or $\# = n+$ for an implicit resolution. Here, we choose an explicit scheme for sake of simplicity. Whatever the choice made, we can update the acoustic variables ρ , $\rho \mathbf{u}$ and ρE. $\theta_{jk}^n = \min\left(u_{jk}^* / \max\left(c_j^n, c_k^n\right), 1\right)$ is the low Mach

correction. This correction makes the accuracy of the full scheme independent of the Mach number. The CFL condition that there is no wave interaction between the Riemann problem at each phase is:

$$\Delta t_{acous}\mathcal{L}_{jk}\max(\tau_k a_k, \tau_j a_j) \leq \frac{1}{2}. \tag{20}$$

where Δt_{acous} is the restriction on time step related to the acoustic subsystem. More details can be found in the work of [1, 3].

3.1.4 Transport subsystem discretization

As a precise interface description is highly requested for two-phase flow simulations, the level set advection will be treated independently with a high-order scheme and will be introduced later. We write the transport subsystem with the conservative variables which causes conservative terms to appear:

$$\begin{cases} \partial_t \rho + \nabla\cdot(\rho\mathbf{u}) - \rho\nabla\cdot\mathbf{u} = 0, \\ \partial_t(\rho\mathbf{u}) + \nabla\cdot(\rho\mathbf{u}^2) - \rho\mathbf{u}\nabla\cdot\mathbf{u} = \mathbf{0}, \\ \partial_t(\rho E) + \nabla\cdot(\rho E\mathbf{u}) - \rho E\nabla\cdot\mathbf{u} = 0. \end{cases}$$

We discretize this system by using the result of the previous acoustic step and with an upwind scheme. The speed used in the upwind scheme needs to be defined at the cell face, so we choose to reuse u^*_{jk}. Then we have the scheme:

$$W_j^{n+1-} = W_j^{n+} - \Delta t \sum_{k\in\mathcal{N}_j} \mathcal{L}_{jk} u^*_{jk} W^{n+}_{jk} + \Delta t W_j^{n+} \sum_{k\in\mathcal{N}_j} \mathcal{L}_{jk} u^*_{jk},$$

where

$$W = (\rho, \rho\mathbf{u}, \rho E)^T, \tag{21}$$

and

$$W^{n+}_{jk} = \begin{cases} W_j^{n+} & u^*_{jk} \geq 0, \\ W_k^{n+} & u^*_{jk} < 0. \end{cases} \tag{22}$$

By combining the discretization of acoustic and transport subsystems, we recover a conservative scheme for the whole Euler system. For a transport subsystem discretized by an upwind scheme (including Level-Set advection), the CFL condition that is only related to the intermediate velocity u^* can be given by:

$$\Delta t_{trans}\mathcal{L}_{jk}|u^*| \leq \frac{1}{2} \tag{23}$$

At low-Mach regime, this constraint on time step Δt_{trans} is less restrictive compared to the acoustic phenomena.

3.1.5 Diffusion subsystem discretization

As the diffusion terms does not have any effect on stability and conservation of the scheme, to avoid a large stencil and a complex splitting, we separate the diffusion subsystem from the global system and the discretization of the diffusion terms is based on the variable at time n. We solve the diffusion terms by using the classical finite volume method. The viscous tensor and thermal diffusion term are discretized with a classical centered second-order scheme.

A classical time-step constraint accounting for the stability conditions on viscosity and heat transfer could be given as followings:

$$\Delta t_{visc} \leq \frac{\Delta x^2 \rho}{\mu} \tag{24}$$

$$\Delta t_{heat} \leq \frac{\rho C_p \Delta x^2}{\mathcal{K}} \tag{25}$$

3.2 Interface coupling

Once the numerical solver for the bulk flow is defined, we now present the coupling between two different fluids for the acoustic and transport subsystems. Using the same technique of splitting, we can get the same subsystems, but here the capillary effects which exist at interface should be taken into account. To keep the equilibrium properties of the numerical scheme, we add the capillary source terms in the acoustic subsystem in an equivalent way as for the gravitational source terms.

3.2.1 Coupling for acoustic subsystem

We start with an acoustic system without gravitational source term, the system can be given by:

$$\begin{cases} \partial_t \tau - \tau \nabla \cdot \mathbf{u} = 0, \\ \partial_t \mathbf{u} + \tau \nabla \pi = \tau M \nabla \phi, \\ \partial_t E + \tau \nabla \cdot (\pi \mathbf{u}) = \tau M \mathbf{u} \cdot \nabla \phi, \\ \phi_t = 0, \end{cases} \tag{26}$$

with $M = \sigma \kappa \delta(\phi) / |\nabla \phi|$. In order to take into account very different properties of each fluid, we perform the same relaxation as in section 3.1.3. Considering the relaxed system:

$$\begin{cases} \partial_t \tau - \tau \nabla \cdot \mathbf{u} = 0, \\ \partial_t \mathbf{u} + \tau \nabla \pi = \tau M \nabla \phi, \\ \partial_t E + \tau \nabla \cdot (\pi \mathbf{u}) = \tau M \mathbf{u} \cdot \nabla \phi, \\ (\pi / a^2)_t + \tau \nabla \cdot \mathbf{u} = 0, \\ a_t = 0, \\ \phi_t = 0. \end{cases} \tag{27}$$

Let (u, v, w) be the fluid velocity vector in the coordinate (x, y, z). Supposing a one-dimensional problem in the direction of x, we have $\rho(x,t)\partial_t \approx \rho(x, t^n)\partial_t$, then

if we define the mass variable m by $\frac{dm(x)}{dx} = \rho(x, t^n)$, we obtain up to a slight abuse of notation, a system that is written in vector form: $\partial_t W + A\partial_m W = 0$, where

$$W = \begin{bmatrix} \tau \\ u \\ \pi \\ E \\ a \\ v \\ w \\ \phi \end{bmatrix}, A = \begin{bmatrix} 0 & -1 & 0 & 0 & 0 & 0 & 0 & 0 \\ 0 & 0 & 1 & 0 & 0 & 0 & 0 & -M \\ 0 & a^2 & 0 & 0 & 0 & 0 & 0 & 0 \\ 0 & \pi & u & 0 & 0 & 0 & 0 & -Mu \\ 0 & 0 & 0 & 0 & 0 & 0 & 0 & 0 \\ 0 & 0 & 0 & 0 & 0 & 0 & 0 & 0 \\ 0 & 0 & 0 & 0 & 0 & 0 & 0 & 0 \\ 0 & 0 & 0 & 0 & 0 & 0 & 0 & 0 \end{bmatrix},$$

and

$$\det(A - \lambda \mathcal{I}d) = -\lambda^6(\lambda^2 - a^2).$$

The matrix A is diagonalizable and its eigenvalues are: $-a$, 0, a. Fields involved in this system are all linearly degenerated. Considering a discontinuity that propagates at celerity D, let [b] be the jump of the variable b across the interface. Following the Rankine-Hugoniot relationships we get the jump conditions:

$$\begin{cases} -D[\tau] - [u] = 0, & \text{(28a)} \\ -D[u] + [\pi] - q[\phi] = 0, & \text{(28b)} \\ -D[E] + [\pi u] - q'[\phi] = 0, & \text{(28c)} \\ -D[a] = 0, & \text{(28d)} \\ -D[v] = 0, & \text{(28e)} \\ -D[w] = 0, & \text{(28f)} \\ -D[\phi] = 0, & \text{(28g)} \end{cases}$$

with D has the same value as eigenvalues of matrix A. q and q' are weights associated with the Dirac mass M and Mu, their definition will be given later. $D = 0$ yields that u is a independent Riemann invariant for the wave $\lambda = 0$ and brings in the jump conditions $[\pi] = q[\phi]$ and $[a] \in \mathbf{R}$ in (28c) and (28d). Thus a is not necessary to be continuous across the wave $\lambda = 0$, and the jumps condition of π should conform to the Laplace equation (6).

Associated Riemann problem

We now consider the Riemann problem associated with the set of equations (28). The solution of the Riemann problem relies on a three-wave structure as depicted in Fig. 1 involving two intermediate states W_l^* and W_r^*. Using the jump relations (28) we can fully determine W_l^* and W_r^*.

First the jump conditions across the wave $\lambda = 0$ imply that $\pi_r^* - \pi_l^* = q(\phi_r - \phi_l)$ and $u^* = u_l^* = u_r^*$. Then the jump conditions (28b) across the waves $-a_l$ and a_r give:

$$\begin{array}{l} a_l(u^* - u_l) + \pi_l^* - \pi_l = 0, \\ a_r(u_r - u^*) - \pi_r - \pi_r^* = 0. \end{array} \quad (29)$$

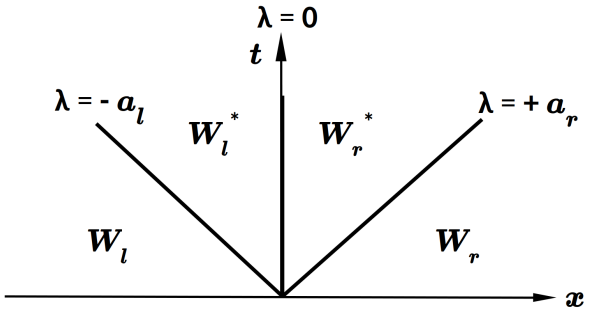

Fig. 1 Wave structure of a Riemann problem at interface for two-phase flow

By solving (29), we get u^* and π^*:

$$
\begin{aligned}
u^* &= \frac{a_l u_l + a_r u_r}{a_l + a_r} - \frac{\pi_r - \pi_l}{a_l + a_r} + \frac{q(\phi_r - \phi_l)}{a_r + a_l}, \\
\pi_l^* &= \frac{(a_l \pi_r + a_r \pi_l)}{a_l + a_r} - \frac{a_l a_r [u_r - u_l]}{a_l + a_r} - \frac{q(\phi_r - \phi_l) a_l}{a_r + a_l}, \\
\pi_r^* &= \frac{(a_l \pi_r + a_r \pi_l)}{a_l + a_r} - \frac{a_l a_r [u_r - u_l]}{a_l + a_r} + \frac{q(\phi_r - \phi_l) a_r}{a_l + a_r},
\end{aligned}
$$

The parameter a and CFL condition for the interface coupling are defined in the same way as for the bulk flow introduced in section 3.1.3. Assuming the jumps condition across the wave $\lambda = 0$ for the pressure can be expressed as: $p_r - p_l = \sigma\kappa$, we get the definition of q and q':

$$
q = \sigma\kappa/(\phi_r - \phi_l), \quad q' = u^* \sigma\kappa/(\phi_r - \phi_l). \tag{30}
$$

κ should be evaluated at the interface between cell r et l to guarantee the equilibrium properties of the numerical scheme, its discretization will be introduced in section 4.4. The stability constraint on time step related to the surface tension effects could be expressed as [2]:

$$
\Delta t_{st} \leq \sqrt{\frac{(\rho_1 + \rho_2)\Delta x^3}{4\pi\sigma}} \tag{31}
$$

In order to get a well-balanced scheme for the external source, the modified approximate Riemann solver takes into account the source term in a consistent way as the solver for bulk flow. To eliminate numerical oscillations and preserve equilibrium for cases where the interface does not coincide with the cell face, the potential energy $\rho\psi$ is estimated by using the interface position as a reference that takes the density discontinuity into account. We want our scheme to strictly preserve the equilibrium steady solutions, that are the states satisfying (14). The approximated system of the Riemann problem being solved at the interface instead of at the cell face, then the interface velocity u^* can be corrected by:

$$
u^* = \frac{a_l u_l + a_r u_r}{a_r + a_l} - \frac{\pi_r - \pi_l}{a_r + a_l} - \rho_{lr} \frac{\psi_r - \psi_l}{a_r + a_l} + \frac{\sigma\kappa}{a_r + a_l}. \tag{32}
$$

Here, the $\rho_{lr} = |\phi_l|\rho_l + |\phi_r|\rho_r / |\phi_l - \phi_r|$ is no more an average between ρ_l and ρ_r as presented in (19) but a density-weighted by the ϕ values of each cell. π^* is also solved at the interface by the Riemann problem. The pressure is then extrapolated constantly to the cell face by taking the potential energy into account to satisfy the condition (14) and the pressure at the cell face for cell r can be given by:

$$\pi_r^* = \frac{(a_l \pi_r + a_r \pi_l)}{a_l + a_r} - \frac{\theta a_l a_r}{a_l + a_r}(u_r - u_l) - \rho'_{lr} a_r \frac{\psi_r - \psi_l}{a_l + a_r} + \frac{\sigma \kappa a_r}{a_l + a_r}, \tag{33}$$

where $\rho'_{lr} = \rho_{lr} - \frac{a_l + a_r}{2a_r}\rho_r$, θ is the low-Mach correction as presented in (17) and the source term in (19) for the cell r is discretized as:

$$(\rho \nabla \psi)_{rl} = \rho_r \mathcal{L}_{rl} (\psi_l - \psi_r) \mathbf{n}_{rl}. \tag{34}$$

For a multi-dimensional configuration, normal velocity u_n should be continuous (without phase change) across the interface since the interface is advected by fluid normal velocity as in (5). To ensure continuous u_n^* at interface, we use u_n at two neighboring cells of different fluids to solve the Riemann problem presented in (29): it provides an approximate normal velocity at interface u_n^*. Then velocity u^* normal to the cell face is reconstructed with interface normal velocity u_n^* to update equation (16). However, resolving the associated Riemann problem at the direction normal to the interface could lead to a stability problem as presented in [25]. For the test-case "static bubble" presented in section 5.3, the scheme stability is of importance. We resolve the Riemann in the direction normal to the cell face as the interface is shifted to the cell boundary, the direction of shifted interface and the resolved Riemann problem direction are then consistent.

As sketched in Fig. 2, cells j and k are belonging to two different fluids, this procedure can be split into the following steps to update j cell:

- Compute velocity normal to interface at each cell:

$$u_{j,n} = \mathbf{u}_j \cdot \mathbf{n} \qquad u_{k,n} = \mathbf{u}_k \cdot \mathbf{n},$$

- Solve associated Riemann problem with (32) and (33) then get interface normal velocity u_n^* and π^*.
- Construct velocity normal to cell face u_j^* for j cell:

$$u_j^* = \left(u_n^* \mathbf{n} + \sum_{m=1}^{N-1} (\mathbf{u}_j \cdot \mathbf{t}_m) \mathbf{t}_m \right) \cdot \mathbf{n}_{jk} \tag{35}$$

  where $\mathbf{t}_m$ are tangential vectors at interface and N is the space dimension.
- Update equation (16) for j cell with u_j^* and π^*.

3.2.2 Coupling for transport subsystem

The transport subsystem is discretized with conservative terms that are treated with an upwind scheme. In order to avoid mixed cells, we here define a ghost state based on the cells belonging to another fluid next to the interface and we use the ghost state to discretize the conservative term in the transport step.

For example, as presented in Fig. 2, cell j and cell k with real states of fluid 1 and of fluid 2 respectively are separated by an interface ζ. If the interface velocity

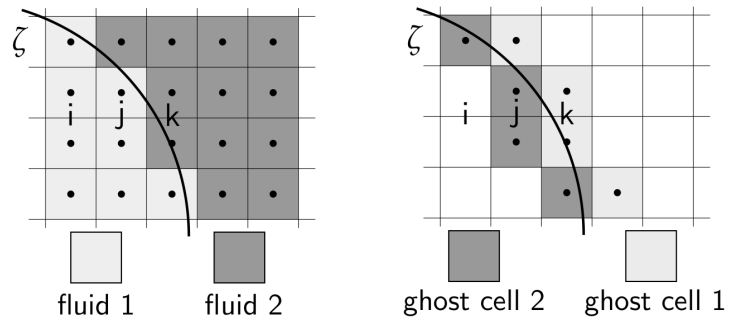

Fig. 2 Ghost cell representation

u^*_{jk} is opposite to the direction of $\mathbf{n}_{jk}$, the upwind flux is then computed with the ghost state in cell k. Then (22) can be modified as:

$$W^{n+}_{jk} = \begin{cases} W^{n+}_{j} & u^*_{jk} \geq 0, \\ W^{n+}_{k,ghost} & u^*_{jk} < 0. \end{cases} \tag{36}$$

The ghost states in cells next to the interface is defined by constant extrapolation [12] in the normal direction:

$$W_t \pm \mathbf{n} \cdot \nabla W = 0. \tag{37}$$

The sign $+$ or $-$ allows us to adjust the direction of propagation. To populate ghost cells in the region where $\phi > 0$, we propagate the real fluid states in the cells of $\phi < 0$ by using the sign $+$. The sign $-$ is used to propagate the real fluid states in the cells of $\phi > 0$ to populate ghost cells in the region where $\phi < 0$. In order to take gravitational potential into account, variable p in ghost cells is also revised by including the contribution of ψ.

3.2.3 Coupling for diffusion subsystem

For the diffusion terms, at the interface, we take the same numerical scheme as section 3.1.5 for discretization. To guarantee the continuity of the tangential constraint at the discrete level, we use the harmonic mean viscosity to evaluate the dynamic viscosity at the interface.

In the present work, we do not take the phase change into account. With assumption of no phase transition, the heat flux across the interface should be continuous. For two cells j and k separated by an interface as presented in Fig. 2, the continuity of heat flux imposes the following relationship:

$$\mathcal{K}_j \frac{T_j - T_I}{\Delta x_j} = \mathcal{K}_k \frac{T_I - T_k}{\Delta x_k}, \tag{38}$$

where Δx_j and Δx_k are the distance to the interface for cell i and for cell k respectively. Estimation of these two distance can be given by:

$$\Delta x_j = \frac{|\phi_j|}{|\phi_j - \phi_k|}\Delta x \quad \Delta x_k = \frac{|\phi_k|}{|\phi_j - \phi_k|}\Delta x. \tag{39}$$

Δx is the mesh size. With (38) and (39), we can give a prediction to the temperature T_I at the interface between cell j and cell k.

3.2.4 Interface movement

As the interface is advected by the fluid velocity field, the value of ϕ evolves with time and may change its sign. For the cell that changes its sign, its real state is replaced by the ghost state in that cell.

4 Interface description

The interface capture is a key point of two-phase flow simulation. In order to have a precise description of the evolution of the interface, We here apply a high-order scheme for level set advection rather than the first-order scheme employed for the transport subsystem.

The numerical methods for level set advection can be divided into two families: the coupled time-space approach and the method of lines (a separate time-space approach). In this work, the retained schemes for the first family are OS (One-Step) type schemes [7]. For the second family of separate approach, WENO [21] and HOUC [26] type spatial discretizations are coupled with Runge-Kutta [15] time discretization.

We start this section by introducing the OS scheme for the level set advection, and then several classical academic test-cases will be applied to compare the OS scheme with the classical separate time-space approaches.

4.1 One-Step scheme for the level set advection

Firstly, we consider the one-dimensional problem:

$$\partial_t \phi + u \partial_x \phi = 0. \tag{40}$$

The Cauchy-Kowalewski procedure applied to (40) reads:

$$\partial_t^k \phi = (-u)^k \partial_x^k \phi, \qquad 0 \leq k \leq n. \tag{41}$$

Supposing u is positive, Taylor series analysis of ϕ at point (x_i, t_n) lead to:

$$\begin{aligned}
\partial_x \phi &= \frac{\phi_i^n - \phi_{i-1}^n}{\Delta x} - \sum_{k=2}^{N} \frac{(-\Delta x)^{k-1}}{k!} \partial_x^k \phi + O(\Delta x^N), \\
\partial_t \phi &= \frac{\phi_i^{n+1} - \phi_i^n}{\Delta t} - \sum_{k=2}^{N} \frac{\Delta t^{k-1}}{k!} \partial_t^k \phi + O(\Delta t^N), \\
&= \frac{\phi_i^{n+1} - \phi_i^n}{\Delta t} + u \sum_{k=2}^{N} \frac{(-\nu \Delta x)^{k-1}}{k!} \partial_x^k \phi + O(\Delta t^N),
\end{aligned} \tag{42}$$

where N signifies the order of accuracy, ν is the CFL number $\nu = |u|\Delta t/\Delta x$. Then by inserting two sub-equations (42) into equation (41), we can get:

$$\begin{aligned}\partial_t\phi + u\partial_x\phi =& \frac{\phi_i^{n+1} - \phi_i^n}{\Delta t} + u_i^n \frac{\phi_i^n - \phi_{i-1}^n}{\Delta x} - u_i^n \sum_{k=2}^{N} \frac{(1-\nu_i^{k-1})(-\Delta x^{k-1})}{k!}\partial_x^k\phi \\ &+ O(\Delta x^N) + O(\Delta t^N).\end{aligned} \tag{43}$$

Let us mention that when $N = 2$ a classical second-order Lax-Wendroff type scheme is recovered as far as a centered finite difference discretization is used for $\partial_x^2\phi$. Following the work of [7], using centered finite difference approximations for even derivatives and upwind approximations for odd derivative depending on the sign of u, the discrete form of the OS scheme recovers a simple expression:

$$\phi_i^{n+1} = \phi^n - u\partial_{x,t}^{N,\pm}\phi + O(\Delta x^N, \Delta t^N), \tag{44}$$

where $\partial_{x,t}^N$ is a numerical discretization of first derivative to ensure N^{th} order of accuracy in time and space, and $\partial_{x,t}^{N,+}$ and $\partial_{x,t}^{N,-}$ are applied for positive and negative u respectively. An arbitrary N^{th} order of accuracy can be obtained by using the odd order accuracy discretization:

$$\partial_{x,t}^{N,\pm}\phi = \frac{1}{\Delta x}\sum_{k=0}^{N} C_k^{N,\pm}\phi_{i\pm k\mp\frac{N+1}{2}}.$$

In the present work, both $N = 5$ and $N = 7$ accuracy orders have been employed. Coefficients C for the fifth accuracy order are:

$$\begin{aligned}
C_0^{5,\pm} &= \pm(\epsilon_4 + \epsilon_5),\\
C_1^{5,\pm} &= \pm(\epsilon_3 - 4\epsilon_4 - 5\epsilon_5),\\
C_2^{5,\pm} &= \pm(-1 + \epsilon_2 - 3\epsilon_3 + 6\epsilon_4 + 10\epsilon_5),\\
C_3^{5,\pm} &= \pm(1 - 2\epsilon_2 + 3\epsilon_3 - 4\epsilon_4 - 10\epsilon_5),\\
C_4^{5,\pm} &= \pm(\epsilon_2 - \epsilon_3 + \epsilon_4 + 5\epsilon_5),\\
C_5^{5,\pm} &= \pm(-\epsilon_5).
\end{aligned}$$

For the seventh order, coefficients are:

$$\begin{aligned}
C_0^{7,\pm} &= \pm(\epsilon_7),\\
C_1^{7,\pm} &= \pm(\epsilon_4 + \epsilon_5 + \epsilon_6 - 7\epsilon_7),\\
C_2^{7,\pm} &= \pm(\epsilon_3 - 4\epsilon_4 - 5\epsilon_5 - 6\epsilon_6 + 21\epsilon_7),\\
C_3^{7,\pm} &= \pm(-1 + \epsilon_2 - 3\epsilon_3 + 6\epsilon_4 + 10\epsilon_5 + 15\epsilon_6 - 35\epsilon_7),\\
C_4^{7,\pm} &= \pm(1 - 2\epsilon_2 + 3\epsilon_3 - 4\epsilon_4 - 10\epsilon_5 - 20\epsilon_6 + 35\epsilon_7),\\
C_5^{7,\pm} &= \pm(\epsilon_2 - \epsilon_3 + \epsilon_4 + 5\epsilon_5 + 15\epsilon_6 - 21\epsilon_7),\\
C_6^{7,\pm} &= \pm(-\epsilon_5 - 6\epsilon_6 + 7\epsilon_7),\\
C_7^{7,\pm} &= \pm(\epsilon_6 - \epsilon_7).
\end{aligned}$$

The ϵ coefficients based on the CFL condition ν are the followings:

$$\begin{aligned} \epsilon_2 &= \frac{1-\nu}{2}, \quad \epsilon_3 = \epsilon_2 \frac{1+\nu}{3}, \quad \epsilon_4 = \epsilon_3 \frac{\nu-2}{4}, \\ \epsilon_5 &= \epsilon_4 \frac{\nu-3}{5}, \quad \epsilon_6 = \epsilon_5 \frac{\nu+2}{6}, \quad \epsilon_7 = \epsilon_6 \frac{\nu+3}{7}. \end{aligned} \tag{45}$$

For a multi-dimension problem, we follow the work of [7] and use a Strang directional splitting strategy. As the signed distance function ϕ is a continuous function, no flux limiter (such as TVD (total variation diminishing) or MP (monotonicity preserving)) is needed in the present scheme.

4.2 Test-cases for level set advection

In order to validate the interface capture level set method, a significant amount of test-cases have been devised over the years of development. Not only can these simulations quantify the performance of the methods, but also help us to put the numerical schemes into practice. Simulation cases called "circle translation", "Zalesak disk" [36] and "Severe interface deformation" are the most often encountered in the literature and are performed with the present schemes to assess their validity. The circle translation test-case simply tests the advection of the scalar distance function with a periodic boundary condition. This test-case allows studying the convergence of the numerical schemes with a smooth initial function. The "Zalesak disk" and "Severe interface deformation" test-cases are calibrated for particular problems, the generation of the ligament in the case of "Severe interface deformation" and the contact angle transport in the case of Zalesak disk. Here, we compare the results between schemes WENO5-RK3, HOUC5/7-RK3 and OS family. In order to evaluate the performance of these numerical schemes, we use two mean errors: global L_1 error computed on the entire domain and local L_1 error computed in a narrow band of width $3\Delta x$ around the interface. This narrow band is of higher interest, as it largely influences the interface precision and the computation of geometric quantities which are important for the hydrodynamic solver. Computations are performed on a personal computer with a 2.80GHz Intel(R) i7-7600U CPU and use double floating-point values (64 bits) in C++ without multi-core parallelism. CPU time t_{cpu} is measured based on an average of at least 100 simulations.

4.2.1 Test-case: Circle advection

In order to study the convergence in two dimensions, here we set the initial function as $\phi(\mathbf{x}_i) = \sqrt{\sum_{i=1}^{2}(x_i - \frac{1}{2})^2} - 0.2$ whose zero-level is a circle of radius 0.2 centered at $(0.5, 0.5)$. This circle is advected in a simple stationary field, non-aligned with cartesian mesh:

$$\begin{cases} u = 1, \\ v = 1. \end{cases} \tag{46}$$

The computation domain is $(x \times y) \in [0,1] \times [0,1]$ with a periodic boundary condition in each direction. The CFL number is set to 0.5 and the errors are measured at $t = 100$ after 100 translations over the domain. As presented in the

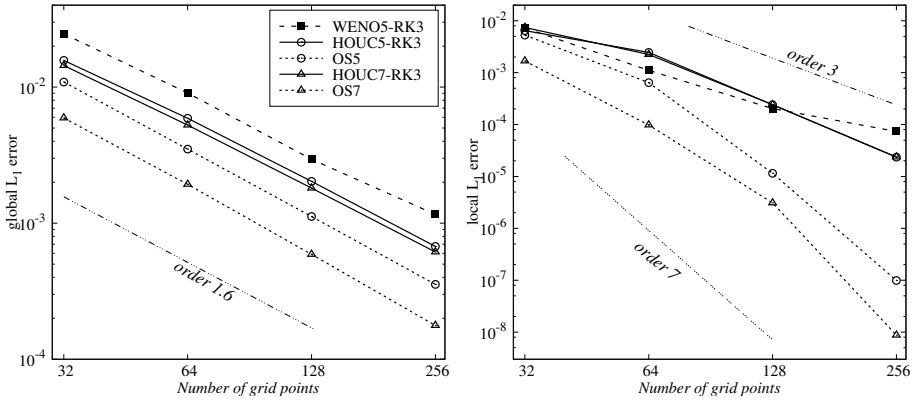

Fig. 3 Spatial Convergence of global (left) and local (right) L_1 errors for circle advection at $t = 100$.

left panel of Fig. 3, all numerical schemes converge, but their order of convergence of the global error is limited to around 1.6 even with a 7^{th} order accurate scheme. Although ϕ is a continuous distance function, its gradient is not always continuous.

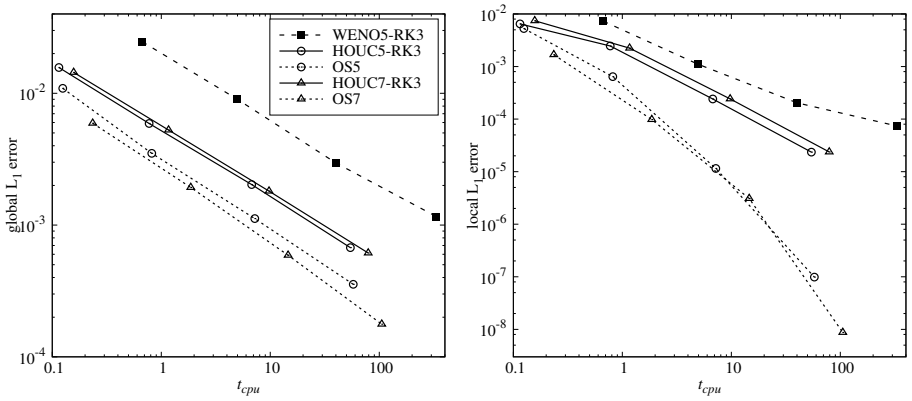

Fig. 4 Global (left) and local (right) L_1 errors versus computation time at $t = 100$ for circle advection (each symbol is a different spatial resolution).

Such discontinuities of $\nabla\phi$ which exist at the boundary and the circle center for the initial function can lower numerical precision of high order scheme. If we are interested in errors close to the interface where there is no discontinuity, local convergence is much faster than the global errors. In the right panel of Fig. 3, we can observe that for the coupled time-space approaches, they reach and almost exceed the theoretical order of accuracy. But for separate time-space, they are limited to an order of accuracy around 3. Numerical errors of separate time-space approach are constrained by $O(\Delta t^3)$ which is the order of Runge-Kutta scheme while errors of OS scheme are constrained by $O(\Delta x^N)$. By reducing time-steps

low below stability condition with RK schemes, we could recover $O(\Delta x^N)$ order of accuracy but at a significantly larger computational cost. When considering

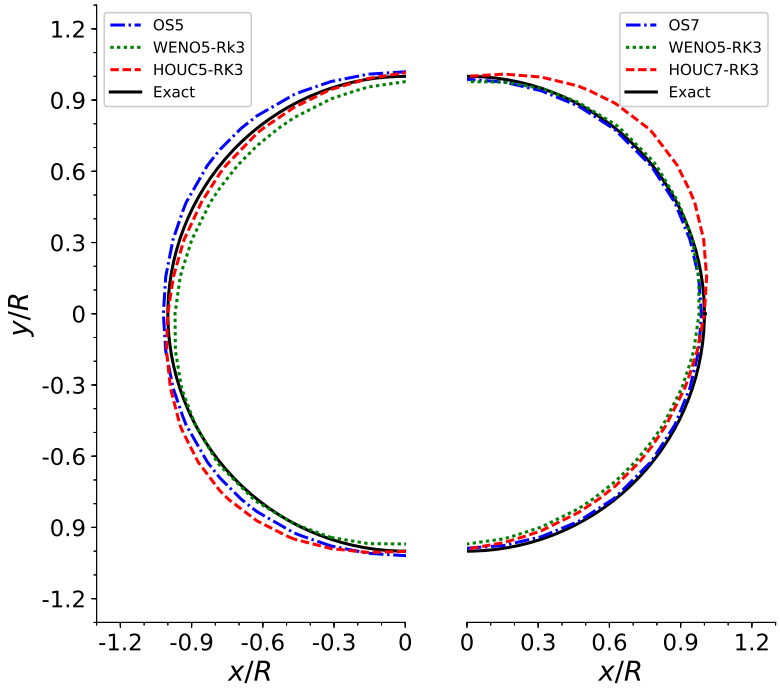

Fig. 5 Zero-level contours of the advected circle for different numerical schemes with a mesh 32×32.

both the errors and computation time, the OS scheme has the best performance. As presented in Fig. 4 where the error is plotted versus the CPU time, curves of both OS5 and OS7 are always below other schemes (for same order) which signifies that OS schemes can give better accuracy for the same computational effort compared to separate time-space approaches.

As presented in Fig. 5, the advected zero level contour of separate time-space approaches is deformed and becomes an ellipse while the zero level contour of coupled time-space approach remains a circle as we paid attention of the operator symmetry in the Strang splitting procedure.

4.2.2 Test-case: Zalesak disk

This test-case consists of the rotation of a rigid body (a disk with a rectangular slot located inside as the exact zero-level contour as presented in Fig. 6). This test presented by [36] is demanding since it could reveal excessive numerical diffusion of schemes, as it presents some very strong local gradients around the slot. The computational domain is a square $[0, 100] \times [0, 100]$; the disk of radius r = 15 is centered on the coordinates (50, 75), the slot is a rectangle [5, 25] located on the vertical diameter of the disk, on its lower part. The rotating velocity field is stationary and defined as

$$\begin{cases} u = \pi(50 - y)/314, \\ v = \pi(x - 50)/314. \end{cases} \tag{47}$$

Disk performs in this field one complete rotation in a dimensionless time t = 628, allowing the superimposition of the numerical solution with its initial state and thus a direct comparison with a subsequent error evaluation. The CFL number is set to 0.5.

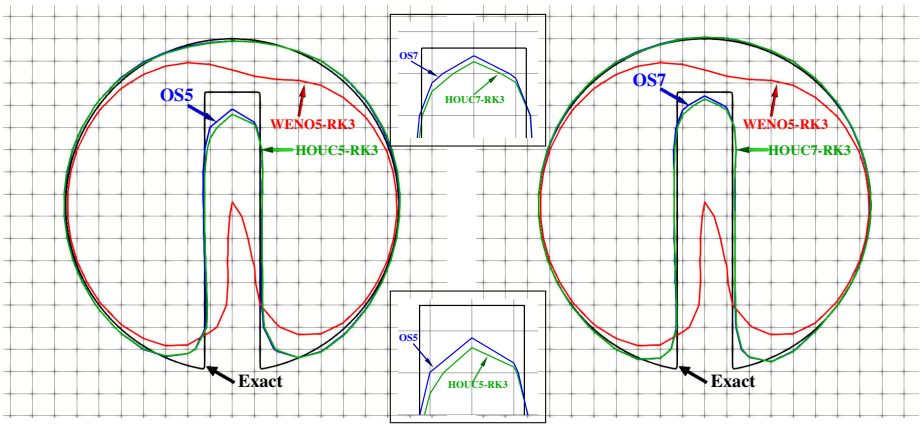

Fig. 6 Results of the Zalesak disk after one full rotation with a resolution of 50×50.

Fig. 6 shows the results of simulation after a full rotation of disk with different schemes with a mesh of 50×50 that corresponds to 2.5 cells in the slot width. The dissipation effects of numerical schemes are shown by the rounding angles of the slot corners. We compare the zero level after a full rotation with the initial contours. We can observe that the WENO5-RK3 method smears the slot severely. For HOUC-RK and OS schemes, corners of the slot are significantly better resolved. When we look at the bottom of the slot, both HOUC-RK and OS schemes have almost the same performance (when comparing schemes at the same order of accuracy of spatial discretization). But when carefully considering the top of the slot, we can observe that this area is slightly better resolved by OS schemes (closer to initial solution).

To quantify the accuracy of these numerical schemes, we use global and local L_1 errors. Results are presented in Fig. 7. We can observe that both global and local

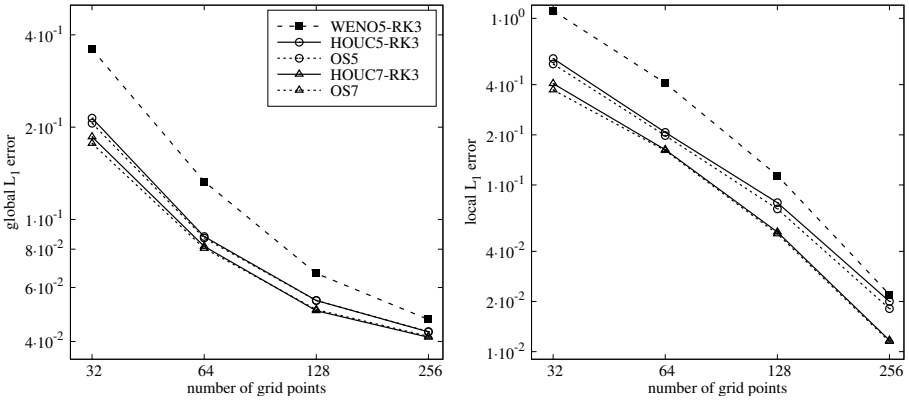

Fig. 7 Global (left) and local (right) L_1 errors for the Zalesak disk rotation

errors of disk advection decrease with mesh refinement but that rate of convergence of global errors also decreases with mesh spacing. It could be explained by the complex geometry of the disk that exhibits sharp corners that lower the accuracy of numerical schemes. For the same type of scheme, the 7^{th} order scheme does not significantly improve solution compared to a 5^{th} order scheme. When comparing methods, we can observe that the WENO5-RK3 scheme results are always less accurate than other schemes with the same order of accuracy. Both OS and HOUC-RK schemes have almost the same accuracy considering global errors.

4.2.3 Test-case: Severe interface deformation

Contrary to previous tests, the velocity field selected in this problem induces the deformation of the initial level set condition. Starting from a circle shape, interface deforms itself in the generation of a long ligament. This case is of high interest since ligament stretches itself indefinitely as time advances: numerical simulation will face an under resolution situation. Numerical methods must be accurate enough to maintain ligament even when its width approaches cell size, and by consequence to maintain initial mass.

A circle of radius $r = 0.15$ is initially centered at point $(0.5, 0.75)$ inside a square domain $[0, 1]^2$. The stationary rotating velocity field is defined by the potential function:

$$\psi = \frac{1}{\pi} sin^2(\pi x) sin^2(\pi y), \tag{48}$$

so that u, v components are defined by

$$\begin{cases} u(x, y) = -2sin^2(\pi x) sin(\pi y) cos(\pi y), \\ v(x, y) = 2sin^2(\pi y) sin(\pi x) cos(\pi x). \end{cases}$$

The CFL number is set to 0.5.

Interface is largely deformed at time $t = 3$ as presented in Fig. 8. The initial circle rolls itself around a central point and transforms into a long ligament. When comparing to the analytical zero-level contours, we can observe that the WENO5-RK3 scheme does not capture interface as much as other schemes do. Both OS

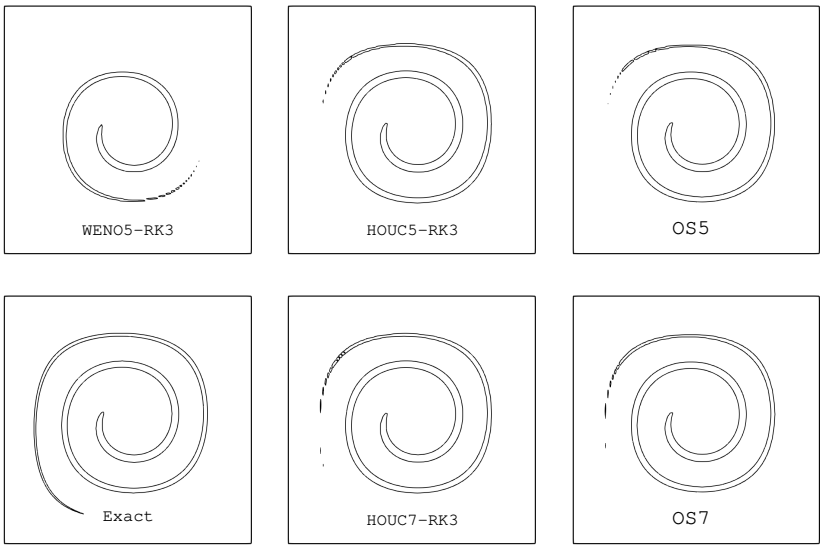

Fig. 8 zero-level contours at $t = 3$. Resolution 100×100 for different numerical schemes and exact solution.

and HOUC-RK schemes with the same order accuracy in space have equivalent interface description accuracy. Temporal surface evolution is presented in Fig. 9: compared to other schemes, surface conservation is less accurate for the WENO5-RK3 scheme. For all schemes, this surface conservation converges as the resolution is increased which will guarantee mass conservation of fluids. For lower resolution, poor mass conservation is a known drawback of the level set method and can be circumvented by coupling to the Volume of fluid method [24].

4.3 level set redistancing

During the level set advection, different isocontours are advected by their local velocities leading to loss of the signed distance property. In consequence, numerical issues arise in the evaluation of normal direction and curvature. In order to circumvent these problems, an additional treatment called 'redistancing' is required to impose the distance function to ϕ. Here, we use an algorithm based on time-dependent Hamilton-Jacobi equation:

$$\begin{aligned} &\frac{\partial \tilde{\phi}}{\partial t'} = \mathrm{sign}(\phi(\mathbf{x}, t))(1 - |\nabla \tilde{\phi}|), \\ &\tilde{\phi}(\mathbf{x}, t' = 0) = \phi(\mathbf{x}, t), \end{aligned} \tag{49}$$

with a steady solution of $|\nabla \phi| = 1$. Equation (49) is then resolved with WENO scheme extended to Hamilton-Jacobi equations [20].

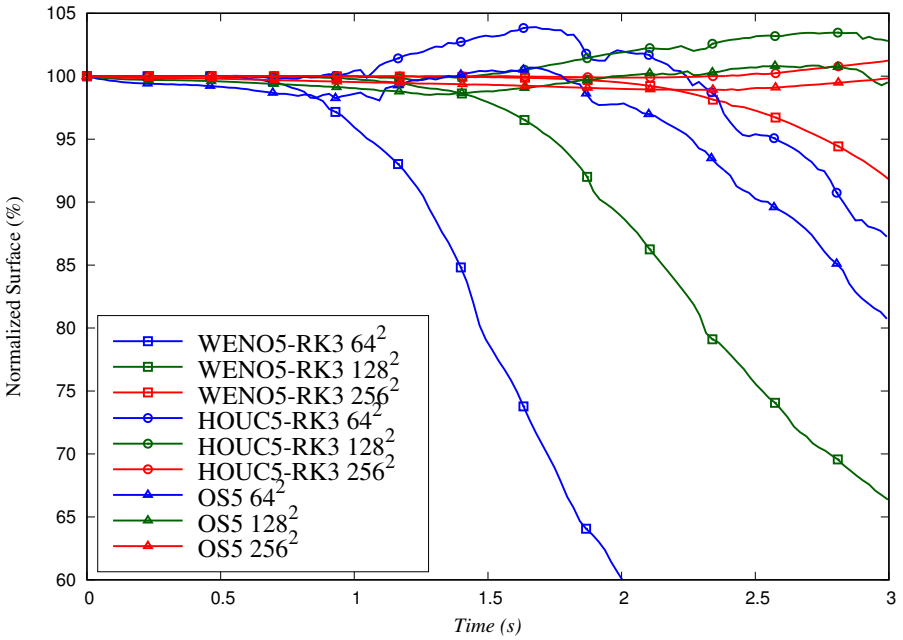

Fig. 9 temporal evolution of surface conservation for deformed circle. Different numerical schemes and resolutions.

4.4 Curvature estimation

As presented in (8), the interface curvature can be deduced directly form the signed distance ϕ and can be evaluated as:

$$\kappa = \frac{\nabla \cdot (\nabla \phi)}{|\nabla \phi|} = \frac{2\phi_x \phi_y \phi_{xy} - \phi_x^2 \phi_{yy} - \phi_y^2 \phi_{xx}}{(\phi_x^2 + \phi_y^2)^{3/2}}. \tag{50}$$

The first and second derivatives are discretized with a centered second-order scheme. As presented in section 3.2.1, κ should be evaluated at the interface between two adjacent cells j and k, its expression can be given as:

$$(\kappa)_{jk} = \frac{\kappa_j |\phi_k| + \kappa_k |\phi_j|}{|\phi_j| + |\phi_k|}. \tag{51}$$

4.5 Time step constraint

By combining (20) (23) (24) (25) and (31), the global time step restriction accounting for acoustic, advection, viscous, heat diffusion and capillary effects can be given as:

$$\Delta t = \min(\Delta t_{acous}, \Delta t_{trans}, \Delta t_{visc}, \Delta t_{heat}, \Delta t_{st}) \tag{52}$$

5 Hydrodynamic numerical test-cases

After previous verification of the correct implementation of the level set advection, we now couple it with hydrodynamic solver adapted to two-phase flows and assess its performance on verification test-cases.

5.1 Two-dimensional sloshing

In this configuration, two non-miscible inviscid fluids of different densities ρ_1 and ρ_2 with $\rho_2 > \rho_1$ are initially at rest in a rectangular tank, the lighter fluid being over the heavier one (see Fig. 10). Gravity g is acting in the vertically downward direction. Then the tank is subjected to a constant horizontal acceleration a_0 with

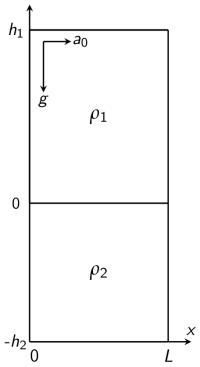

Fig. 10 Sketch of the sloshing tank with acceleration vectors.

$a_0/g = 0.01$. Initial pressure distribution is hydrostatic (reference $p_0 = 10^5$ Pa). Gas is described by an ideal gas law with density $\rho_1 = 1\ \mathrm{kg \cdot m^{-3}}$ and $\gamma_1 = 1.4$. Sound speed in the gas is around $370\ \mathrm{m \cdot s^{-1}}$. Liquid is described by stiffened gas law, with density $\rho_2 = 1000\ \mathrm{kg \cdot m^{-3}}$, $\gamma_2 = 7$ and $p_2^\infty = 3.31 \times 10^8$ Pa. Sound speed in the liquid is around $1500\ \mathrm{m \cdot s^{-1}}$. Gas and liquid heights are $1.25L$ and L respectively with 1 m.

Since a_0/g ratio is small, the interface position can be given analytically by a linear potential approach [5]:

$$\xi = \frac{a_0}{g}\left(x - \frac{L}{2}\sum_{n\geq 0}\frac{4}{Lk_{2n+1}^2}cos(\omega_{2n+1}t)cos(k_{2n+1}x)\right),$$

where $k_n = \frac{\pi n}{L}$ is the wave number, and ω_n can be given by:

$$\omega_{2n+1}^2 = \frac{gk_{2n+1}(\rho_2 - \rho_1)}{\rho_1\ \mathrm{coth}(k_{2n+1}h_1) + \rho_2\ \mathrm{coth}(k_{2n+1}h_2)}.$$

The evolution of computed interface positions on the left and right sides of the tank are compared to analytical solutions, at different spatial resolutions (Fig. 11

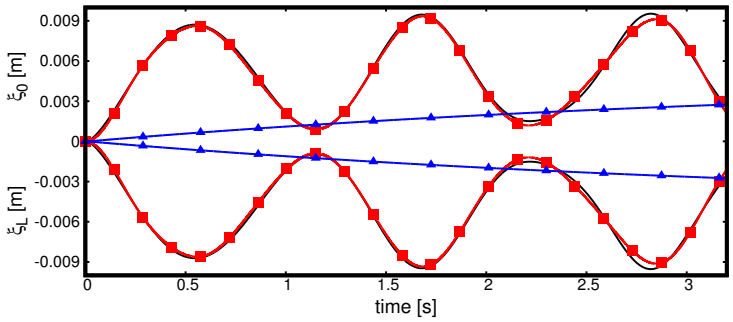

Fig. 11 Temporal evolution of interface at $x = 0$ and at $x = L$ with a uniform mesh 40×90. red line: present method with low-Mach correction; blue line: present method without low-Mach correction; black line: analytical solution.

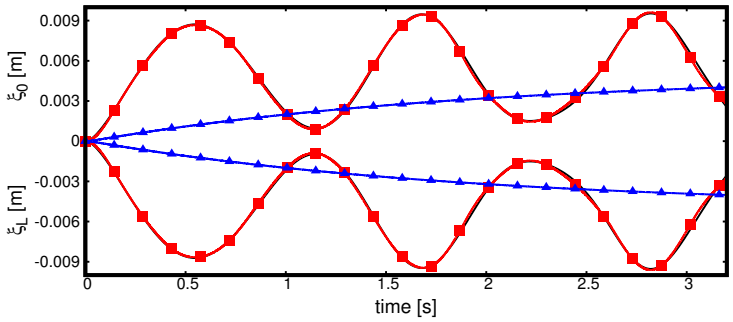

Fig. 12 Temporal evolution of interface at $x = 0$ and at $x = L$ with a uniform mesh 80×180. red line: present method with low-Mach correction; blue line: present method without low-Mach correction; black line: analytical solution.

and Fig. 12). We observe that the present numerical scheme without low-Mach correction is highly dissipative and cannot describe the interface. This is mainly due to the intrinsic dissipation of the scheme (first-order). A posteriori, Mach number of this flow is found to be around 2×10^{-5}: in this low-Mach regime, an adequate numerical scheme is mandatory. Proposed low-Mach correction eliminates excessive numerical dissipation (even without any MUSCL reconstruction) and results coincide with the analytical solution even on a rather coarse mesh.

5.2 Rayleigh-Taylor instabilities

A test-case involving more severe deformation of interface is investigated: "Rayleigh-Taylor instabilities". Accurate numerical description of the interface is needed to follow the complex evolution of interface within this flow. The computation domain is rectangular and filled by two non-miscible fluids of different densities $\rho_1 = 1$ and $\rho_2 = 1.8$. The two layers of fluid are initially superimposed with heavier one over lighter one. Initial interface is perturbed and located at $y = 1 - sin(2\pi x)$. Reynolds number is based on the half-height of the domain and on an equal kinematic viscosity ν for both fluids: $Re = \sqrt{(H/2)^3/g}/\nu = 420$. Ideal gas law is used

for both fluids, with a reference pressure of $p_0 = 400$ and $\gamma = 7$. Mach number of this flow is around 0.01, in the low-Mach regime.

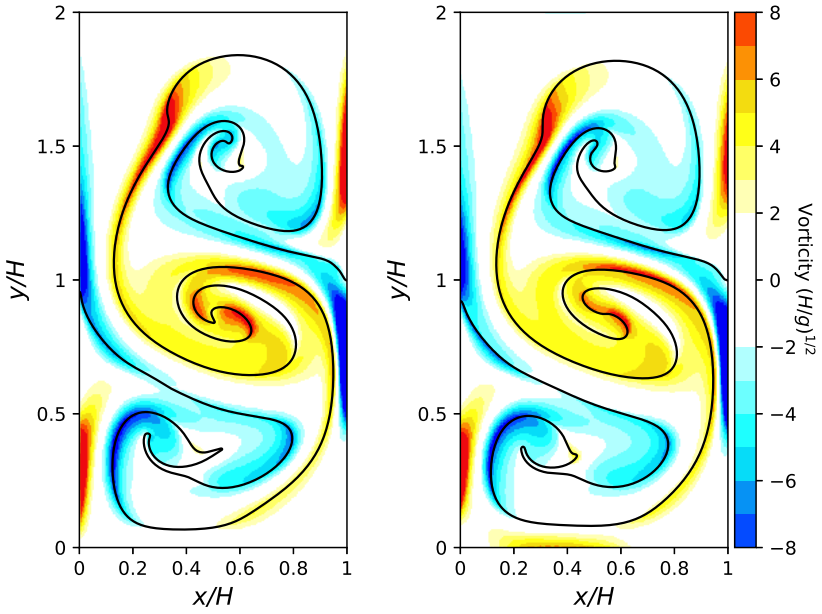

Fig. 13 Vorticity of Rayleigh-Taylor instabilities test-case with a resolution of 320×640 at $t^* = 5$. Left: present compressible level set formulation; Right: incompressible level set formulation [37].

The left figure in Fig. 13 presents interface position and vorticity at $t^* = 5$ for the present compressible level set formulation while the right figure gives a reference solution of an incompressible level set formulation [37] at the same time $t^* = \sqrt{g/H} = 5$. Comparing interface shapes and vorticity patterns presented in Fig. 13, these two methods have similar behavior. Fig. 14 shows the spatial convergence of two different models. Both models converge but the way that they converge is quite different. Numerical results show that the incompressible method converges faster than the compressible method (which is expected as the compressible method is first-order while the incompressible method is second-order) but the main difference exists in the area of high gradients. From this test-case, we can find that in a low-Mach regime, our numerical scheme can well predict the fluid behavior with large deformation.

5.3 Static bubble in equilibrium

To test the convergence of surface tension discretization and well-balanced scheme of the jump condition treatment at the interface, the "static bubble in equilibrium" [13] test is certainly the first case of rudimentary simulation to implement.

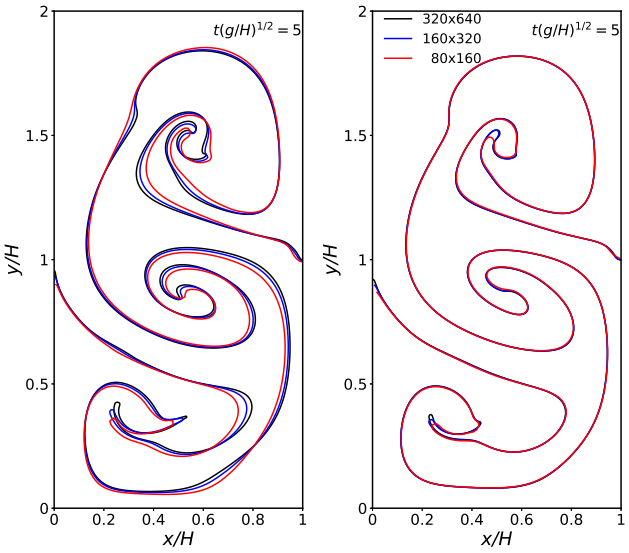

Fig. 14 Spatial convergence of RayleighTaylor instabilities at $t^* = 5$. Left: present compressible level set formulation; Right: incompressible level set formulation [37].

The simplicity of this case of simulation makes it possible to well isolate this phenomenon, the theoretical solution being simply dictated by Laplace's law. As presented in [31], the redistancing step tends to perturb the curvature and prevents the system from reaching an exact balance. For this test-case, this step is not activated.

A 2D bubble with a radius R=0.4 containing an ideal gas is placed in a slightly compressible liquid. The gas is described by an ideal gas law with $\gamma_g = 1.4$ and $p_g^\infty = 0$ while the liquid is described by a stiffened gas law with $\gamma_l = 7.14$ and $p_l^\infty = 300$. The initial densities of these two fluids are equal with $\rho_{g,0} = \rho_{l,0} = 1$. The initial pressure in liquid is $p_{l,0} = 1$. To confirm the Laplace's law, the initial pressure in the gas is given by: $p_{g,0} = p_{l,0} + \frac{\sigma}{R_0}$. The surface tension coefficient σ is set to be 1, and the Laplace number $La = \frac{\rho D_0 \sigma}{\mu^2}$ is set to be 12000.

Fig. 15 and Fig 16 show the spatial convergence of numerical scheme resolutions without and with low-Mach correction respectively. From these two figures, we can find that the initial maximum amplitudes of spurious currents decrease as we refine mesh which shows a good convergence of the numerical scheme. Because of the total viscosity (including numerical viscosity and physical viscosity μ), both of these two models reduce the amplitude of spurious currents to machine precision and a good well-balanced property is observed.

In Fig. 15, without low-Mach correction, the amplitudes of spurious currents reduce at different rates. As mesh refinement has an important influence on numerical viscosity which is proportional to the mesh size, these different rates at different resolutions show the importance of the numerical viscosity compared

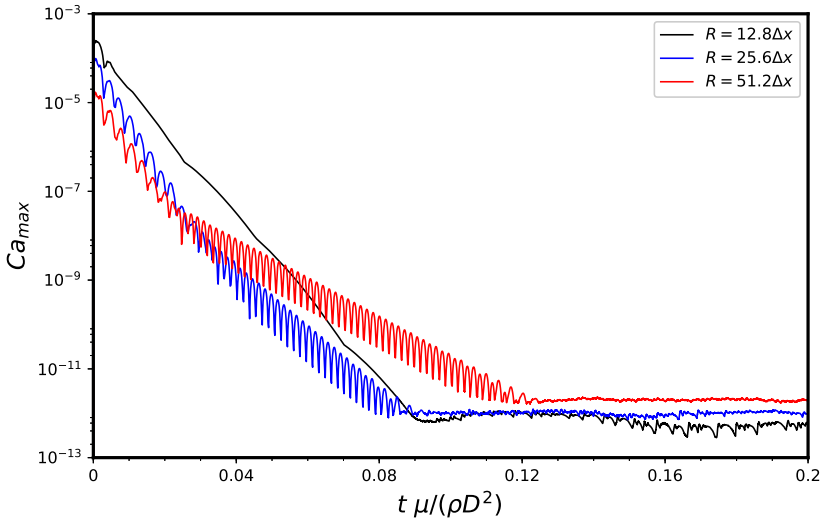

Fig. 15 Temporal evolution of velocity fluctuations of a 2D bubble (La=12000) at different resolutions: without low-Mach correction.

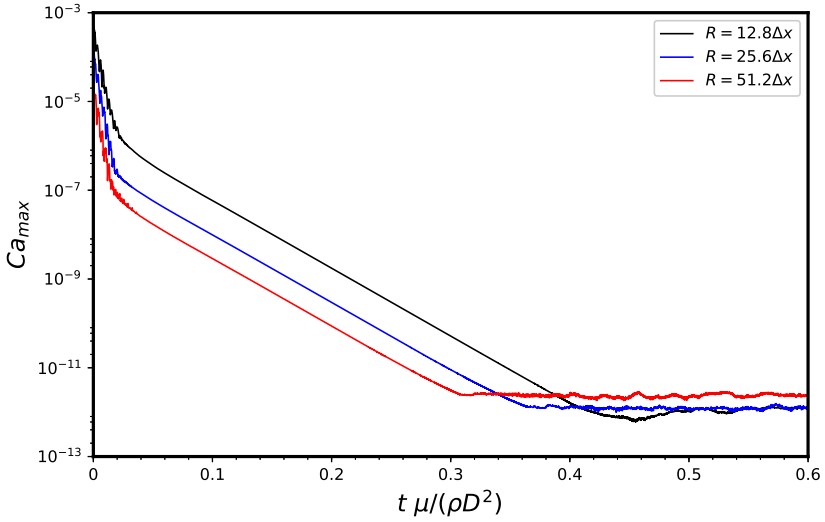

Fig. 16 Temporal evolution of velocity fluctuations of a 2D bubble (La=12000) at different resolutions: with low-Mach correction.

to the physical viscosity μ. In Fig 16, with low-Mach correction, the amplitudes of spurious currents reduce at the same rate. This phenomenon shows that the insignificance of numerical viscosity compared to the physical viscosity and the numerical viscosity is eliminated effectively.

80×160	160×320	320×640
x%	y %	z%

Table 1 Mas loss of Rayleigh-Taylor instabilities of fluid 1 at $t = 5$

As presented in the test-case: "Severe interface deformation"in Section 4.2.3, the Level-Set method can't guarantee the mass conservation. To present the performance of present model on conservation, we give the mass loss of fluid 1 or different mesh at time $t = 5$ in Table 1.

5.4 Rising bubble

In this section, we want to study a more complex flow with surface tension effects, viscous effects, high-density ratio and large interface deformation. For this first problem, we simulate a configuration that has been studied with an incompressible level set method [33]. It is an air bubble rising in a column of water at rest. The domain is shown in Fig. 17. The flow is characterized by the following

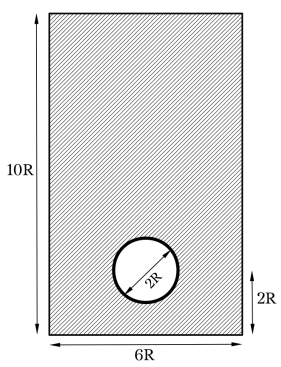

Fig. 17 Sketch of the domain for test-case "rising bubble".

dimensionless numbers: the Reynolds number $Re = \sqrt{(2R)^3 g}\rho_x/\mu_x = 1000$ and the Bond number $Bo = 4\rho_x R^2 g/\sigma$=200. The density ratio is equal to 1000 with $\rho_{g,0} = 1$ and $\rho_{l,0} = 1000$. Both fluids are defined by the following characteristics: for liquid, $\gamma_l = 7.14$, $p_l^\infty = 3.31 \times 10^8$ and the liquid viscosity $\mu_l = 0.035$, for gas, $\gamma_g = 1.4$, $p_g^\infty = 0$ and the gas viscosity $\mu_g = 0.0045$. The bubble radius is equal to 0.025 and the gravity acceleration $g = 9.81$. The reference pressure in the liquid is around 10^5 which gives a sound speed $c_g = 374$ in the gas and $c_l = 1537$ in the liquid. The Mach number in this flow is close to 10^{-3}, in a low-Mach regime.

Numerical results are presented in Fig. 18, the evolution of interface is shown and superposed with reference results [33]. We can find that these two models have similar behavior and the top of interfaces of these two models coincides very well. From $t^* = 4.8$, in the incompressible level set formulation, there are some small bubbles appearing, while with the present model, this phenomenon is not

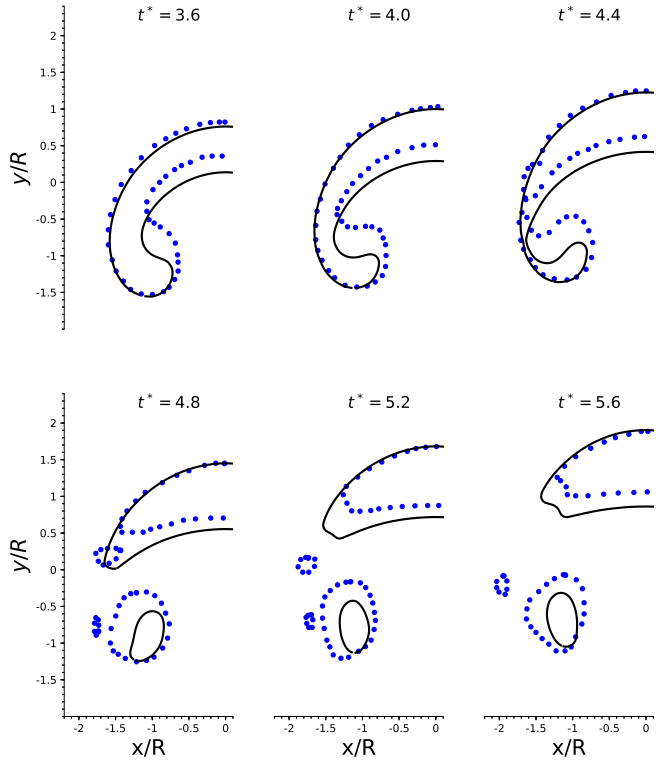

Fig. 18 Interface at different non-dimensional time $t^* = t\sqrt{R/g}$ of present method (black line) and reference (blue circles) [33].

predicted. This test-case is constructed numerically, it is hard to reproduce experimentally. For the phenomenon such as the bubble coalescence and separation, more special treatments are required, such as the curvature estimation. As this problem is not the key issue of the present study, more attention should be paid when studying bubbly flow.

5.5 1D non-isothermal problem

In this test-case, we want to illustrate the interest to simulate low-Mach flows with a compressible solver. In fact, for a flow at low-Mach regime, the compressibility could be important when considering thermal dilatation.

We consider the test-case "1D non-isothermal problem"as in [6]. A closed 1D tube of length 100μm is consisting of a liquid layer of length 10μm between of two layers of air as depicted in Fig. 19. The liquid layer is initially suited at the center

of the tube. The initial pressure and temperature in the system are 101325 Pa and

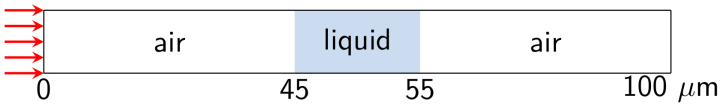

Fig. 19 Sketch of the 1D non-isothermal tube

293.15 K respectively. Both fluids are defined by the following characteristics: for gas, $\gamma_g = 1.4$, $p_g^\infty = 0$, specific heat at constant pressure $c_{pg} = 1004.5$ JK^{-1}kg^{-1}, thermal conductivity $\mathcal{K}_g = 0.0256$ Wm^{-1}K^{-1}, dynamic viscosity $\mu_g = 1.82 \times 10^{-5}$ Pa$\cdot$s. A barotropic liquid with a sound speed of 1500 ms^{-1} is considered, the initial density $\rho_l = 1000$ kg/m^3, specific heat $c_{pl} = 4184$ JK^{-1}kg^{-1}, thermal conductivity $\mathcal{K}_l = 0.6$ Wm^{-1}K^{-1}, dynamic viscosity $\mu_l = 0.001$ Pa$\cdot$s. At initial time, the left wall is heated to $T_w = 373.15$ K and the right wall is insulated.

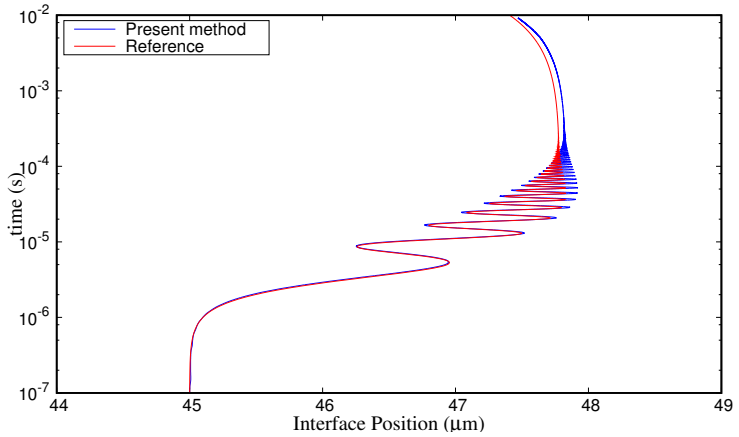

Fig. 20 Trajectory of the interface at left side (resolution: 100 grid points)

The tube is then heated, and the liquid layer start moving. Fig. 20 presents the interface trajectory in the early stages right after the heating of the left wall. An oscillatory motion is observed. This oscillation is entirely related to e gas compressibility as presented in [6]. This phenomenon confirms the importance of compressibility for low-Mach flows prediction. By comparing the interface trajectory with the reference [6], a good agreement could be found.

6 Conclusions

A sharp interface method for two-phase compressible flows at low-Mach regime is presented. Since Mach number could be very small in liquid, classical compressible methods could be very diffusive as the error is inversely proportional to the Mach

number. In order to circumvent such an issue, an accurate low-Mach numerical scheme is used to describe each fluid of two different phases. The interface is captured by a level set method.

To keep an accurate interface description, a new high order coupled time-space approach (OS) is presented for interface advection. Several academic test-cases have been performed to validate this approach and compare it with other well-known approaches. These tests show that the OS scheme is more accurate and efficient, especially for the circle advection test-case.

Then the coupling of the hydrodynamic solver with the interface is realized by the classical ghost fluid method and the interface is treated as a shock-wave discontinuity. Finally, for the final update, each cell is considered as a pure phase: the interface is aligned with grid faces.

After some validations of numerical schemes for level set advection, more extensive test-cases are performed to validate the complete numerical solver. When considering very low Mach flow with high-density ratio, the proposed low Mach correction plays a significant role which drastically reduces numerical diffusion and allows to match inviscid solution (for two-dimensional sloshing test-case).

At higher Mach number (but still with slight compressible effects) and lower density ratio, the proposed solver allows capturing severe interface deformations (in the Rayleigh Taylor instabilities test-case) despite approximation induced by the alignment of interface to cell faces. Upgrade to second-order space discretization will certainly improve the convergence of the scheme.

Finally, surface tension effects are correctly handled by the proposed solver, exhibiting the well-balanced property of the numerical scheme (on the static bubble test-case) and good agreement for dynamical test-case (rising bubble). The test-case "1D non-isotherm problem" enlightens the importance of compressibility for low-Mach flows, and the numerical results coincide well with results in the literature.

Future investigations could focus on improving the numerical properties of the present scheme (discretization order in space, mass conservation properties, implicit scheme for the acoustic subsystem) as well as enlarging physical effects to mass transfer.

Acknowledgements We warmly thank Samuel Kokh, Pascal Tremblin and Thomas Padioleau from Maison de la Simulation for their helpful suggestions and fruitful discussions. Ziqiang Zou is funded by a Ph.D. grant from China Scholarship Council (CSC). We also thank Davide Zuzio to provide incompressible level set numerical results for Rayleigh-Taylor test-case.

Conflict of interest

The authors declare that they have no conflict of interest.

References

1. Bouchut, F.: Nonlinear stability of finite Volume Methods for hyperbolic conservation laws: And Well-Balanced schemes for sources. Springer Science & Business Media (2004)

2. Brackbill, J.U., Kothe, D.B., Zemach, C.: A continuum method for modeling surface tension. Journal of Computational Physics **100**(2), 335–354 (1992)
3. Chalons, C., Girardin, M., Kokh, S.: An all-regime Lagrange-Projection like scheme for the gas dynamics equations on unstructured meshes. Communications in Computational Physics **20**(1), 188–233 (2016)
4. Chalons, C., Kestener, P., Kokh, S., Stauffert, M.: A large time-step and well-balanced Lagrange-projection type scheme for the shallow water equations. Communications in Mathematical Sciences **15**(3), 765–788 (2017)
5. Chanteperdrix, G.: Modélisation et simulation numérique des ecoulements diphasiques à interfaces libres. application à l'étude des mouvements de liquides dans les réservoirs de véhicules spatiaux. Ph.D. thesis, Ecole Nationale Supérieure de l'Aéronautique et de l'Espace (2004)
6. Daru, V., Le Quéré, P., Duluc, M.C., Le Maitre, O.: A numerical method for the simulation of low Mach number liquid–gas flows. Journal of Computational Physics **229**(23), 8844–8867 (2010)
7. Daru, V., Tenaud, C.: High order one-step monotonicity-preserving schemes for unsteady compressible flow calculations. Journal of computational physics **193**(2), 563–594 (2004)
8. Dellacherie, S.: Analysis of Godunov type schemes applied to the compressible Euler system at low Mach number. Journal of Computational Physics **229**(4), 978–1016 (2010). DOI 10.1016/j.jcp.2009.09.044
9. Desjardins, O., Moureau, V., Pitsch, H.: An accurate conservative level set/ghost fluid method for simulating turbulent atomization. Journal of Computational Physics **227**(18), 8395–8416 (2008)
10. Enright, D., Fedkiw, R., Ferziger, J., Mitchell, I.: A hybrid particle level set method for improved interface capturing. Journal of Computational physics **183**(1), 83–116 (2002)
11. Fechter, S., Munz, C.D., Rohde, C., Zeiler, C.: A sharp interface method for compressible liquid–vapor flow with phase transition and surface tension. Journal of Computational Physics **336**, 347–374 (2017)
12. Fedkiw, R.P., Aslam, T., Merriman, B., Osher, S.: A non-oscillatory Eulerian approach to interfaces in multimaterial flows (the ghost fluid method). Journal of computational physics **152**(2), 457–492 (1999)
13. Fuster, D., Popinet, S.: An all-Mach method for the simulation of bubble dynamics problems in the presence of surface tension. Journal of Computational Physics **374**, 752–768 (2018)
14. Goncalvès, E., Patella, R.F.: Constraints on equation of state for cavitating flows with thermodynamic effects. Applied Mathematics and Computation **217**(11), 5095–5102 (2011)
15. Gottlieb, S., Shu, C.W.: Total variation diminishing Runge-Kutta schemes. Mathematics of computation of the American Mathematical Society **67**(221), 73–85 (1998)
16. Hirt, C.W., Nichols, B.D.: Volume of fluid (VOF) method for the dynamics of free boundaries. Journal of computational physics **39**(1), 201–225 (1981)
17. Houim, R.W., Kuo, K.K.: A ghost fluid method for compressible reacting flows with phase change. Journal of Computational Physics **235**, 865–900 (2013)
18. Hu, X., Adams, N.A., Iaccarino, G.: On the HLLC riemann solver for interface interaction in compressible multi-fluid flow. Journal of Computational Physics **228**(17), 6572–6589 (2009)
19. Hu, X.Y., Khoo, B., Adams, N.A., Huang, F.: A conservative interface method for compressible flows. Journal of Computational Physics **219**(2), 553–578 (2006)
20. Jiang, G.S., Peng, D.: Weighted ENO schemes for Hamilton–Jacobi equations. SIAM Journal on Scientific computing **21**(6), 2126–2143 (2000)
21. Jiang, G.S., Shu, C.W.: Efficient implementation of weighted ENO schemes. Journal of computational physics **126**(1), 202–228 (1996)
22. Lalanne, B., Villegas, L.R., Tanguy, S., Risso, F.: On the computation of viscous terms for incompressible two-phase flows with level set/ghost fluid method. Journal of Computational Physics **301**, 289–307 (2015)
23. Lin, J.Y., Shen, Y., Ding, H., Liu, N.S., Lu, X.Y.: Simulation of compressible two-phase flows with topology change of fluid–fluid interface by a robust cut-cell method. Journal of Computational Physics **328**, 140–159 (2017)
24. Ménard, T., Tanguy, S., Berlemont, A.: Coupling level set/VOF/ghost fluid methods: Validation and application to 3D simulation of the primary break-up of a liquid jet. International Journal of Multiphase Flow **33**(5), 510–524 (2007)

25. Nourgaliev, R.R., Dinh, T.N., Theofanous, T.G.: Adaptive characteristics-based matching for compressible multifluid dynamics. Journal of Computational Physics **213**(2), 500–529 (2006)
26. Nourgaliev, R.R., Theofanous, T.G.: High-fidelity interface tracking in compressible flows: Unlimited anchored adaptive level set. Journal of Computational Physics **224**(2), 836–866 (2007)
27. Olsson, E., Kreiss, G.: A conservative level set method for two phase flow. Journal of computational physics **210**(1), 225–246 (2005)
28. Osher, S., Sethian, J.A.: Fronts propagating with curvature-dependent speed: algorithms based on Hamilton-Jacobi formulations. Journal of computational physics **79**(1), 12–49 (1988)
29. Padioleau, T., Tremblin, P., Audit, E., Kestener, P., Kokh, S.: A High-performance and Portable All-Mach Regime Flow Solver Code with Well-balanced Gravity. Application to Compressible Convection. The Astrophysical Journal **875**(2), 128 (2019)
30. Paolucci, S.: On the Filtering of Sound from the Navier-Stokes equations. Tech. Rep. 82-8257, Sandia National Laboratories (1982)
31. Popinet, S.: Numerical models of surface tension. Annual Review of Fluid Mechanics **50**, 49–75 (2018)
32. Saurel, R., Abgrall, R.: A multiphase Godunov method for compressible multifluid and multiphase flows. Journal of Computational Physics **150**(2), 425–467 (1999)
33. Sussman, M., Smereka, P., Osher, S.: A level set approach for computing solutions to incompressible two-phase flow. Journal of Computational physics **114**(1), 146–159 (1994)
34. Toro, E.F.: Riemann solvers and numerical methods for fluid dynamics: a practical introduction. Springer Science & Business Media (2013)
35. Unverdi, S.O., Tryggvason, G.: A front-tracking method for viscous, incompressible, multi-fluid flows. Journal of computational physics **100**(1), 25–37 (1992)
36. Zalesak, S.T.: Fully multidimensional flux-corrected transport algorithms for fluids. Journal of computational physics **31**(3), 335–362 (1979)
37. Zuzio, D., Estivalezes, J.: An efficient block parallel AMR method for two phase interfacial flow simulations. Computers & Fluids **44**(1), 339–357 (2011)